RSC Advances

PAPER

View Article Online
View Journal | View Issue

Cite this: *RSC Adv.*, 2017, **7**, 25685

Luminescence properties and site occupancy of Ce^{3+} in Ba_2SiO_4: a combined experimental and *ab initio* study†

Litian Lin,[a] Xiaoxiao Huang,[b] Rui Shi,[a] Weijie Zhou,[a] Yan Huang,[c] Jiuping Zhong,[a] Ye Tao,[c] Jun Chen,[d] Lixin Ning*[b] and Hongbin Liang*[a]

Photoluminescence properties of $Ba_{2-2x}Ce_xNa_xSiO_4$ ($x = 0.0005$) prepared by a solid-state reaction method are first studied with excitation energies in the vacuum-ultraviolet (VUV) to ultraviolet (UV) range at low temperature. Five bands are observed in the excitation spectrum of Ce^{3+} 5d → 4f emission at 26.5 K. The highest energy band is attributed to the host excitonic absorption, from which the band gap energy of the host is estimated to be around 7.36 eV. The four lower energy bands are assigned to the 4f → 5d transitions of Ce^{3+} located at one of the two types of Ba sites in Ba_2SiO_4, based on a comparison of excitation spectra at different monitoring wavelengths. Under UV excitation, the material exhibits bright luminescence at 350–450 nm, with a fast decay time (~26 ns at 4 K) and a high thermal quenching temperature (>500 K). In view of this, X-ray excited luminescence measurements are then conducted, and the results suggest a potential application of Ba_2SiO_4:Ce^{3+} as scintillation phosphors. Hybrid density functional theory (DFT) calculations within the supercell model are carried out to optimize the local structures of Ce^{3+} at the two Ba sites in Ba_2SiO_4, on which wave function-based *ab initio* embedded cluster calculations are performed to derive the $4f^1$ and $5d^1$ energy levels of Ce^{3+}. On the basis of the calculated DFT total energies and the comparison between experimental and calculated 4f → 5d transition energies, we find that the luminescence originates predominantly from Ce^{3+} occupying nine-coordinated Ba2 sites. Furthermore, electronic properties of Ce^{3+} in Ba_2SiO_4 are evaluated to provide an understanding of the high thermal stability of the 5d luminescence at the level of electronic structures.

Received 12th April 2017
Accepted 9th May 2017

DOI: 10.1039/c7ra04145d

rsc.li/rsc-advances

1. Introduction

Silicate compounds have been considered as suitable hosts of lanthanide ions for applications as luminescent materials due to their good chemical stability, low manufacturing cost, and environment-friendly characteristics.[1] Recently, alkaline earth orthosilicate phosphors, M_2SiO_4:Ce^{3+}, Eu^{2+} (M = Ca, Sr, Ba) have received renewed interest due to their potential use as phosphors in white light-emitting diodes (LEDs),[2–5] although they were first reported more than four decades ago.[6,7] A significant feature of this class of phosphors is the ease of tuning the emission wavelength by changing the composition of M cations or by manipulating the crystalline polymorphism. For instance, the emission color of $Sr_xBa_{2-x}SiO_4$:Eu^{2+} can be varied from green for Ba_2SiO_4:Eu^{2+} to yellow for Sr_2SiO_4:Eu^{2+},[8] and Ca_2SiO_4:Ce^{3+} exhibited yellow emission in the γ-phase and light-blue emission in the β-phase.[9] The light emission originates from spin- and parity-allowed 5d → 4f transition of Eu^{2+} or Ce^{3+}, and the transition energy depends strongly on the geometric structure of the local environment due to the large crystal-field interaction of the 5d electron with its surroundings.[10]

Among the alkaline earth orthosilicates, Ba_2SiO_4 stabilizes only in an orthorhombic structure with the space group *Pmcn* (no. 62), having two crystallographically distinct Ba sites (Ba1 and Ba2 sites) of C_s symmetry (Fig. 1a).[11] Within a distance of 3.3 angstrom, the Ba1 and Ba2 sites are coordinated by ten and nine oxygen atoms, respectively. Activated by Ce^{3+}, the material displays intense emission at around 384 nm under UV excitations,[7] but the location of Ce^{3+} on the Ba1 or Ba2 site is not yet clear. When Ca_2SiO_4 was added to Ba_2SiO_4 *via* solid solution, the emission band shifted to longer wavelengths, at around 400 nm for $Ba_{1.2}Ca_{0.8}SiO_4$:Ce^{3+} with a high thermal quenching

[a]MOE Key Laboratory of Bioinorganic and Synthetic Chemistry, KLGHEI of Environment and Energy Chemistry, School of Chemistry, Sun Yat-sen University, Guangzhou 510275, China
[b]Anhui Province Key Laboratory of Optoelectric Materials Science and Technology, Department of Physics, Anhui Normal University, Wuhu, Anhui 241000, China
[c]Beijing Synchrotron Radiation Facility, Institute of High Energy Physics, Chinese Academy of Sciences, Beijing 100039, China
[d]School of Electronics and Information Technology, Sun Yat-sen University, Guangzhou 510275, China

† Electronic supplementary information (ESI) available. See DOI: 10.1039/c7ra04145d

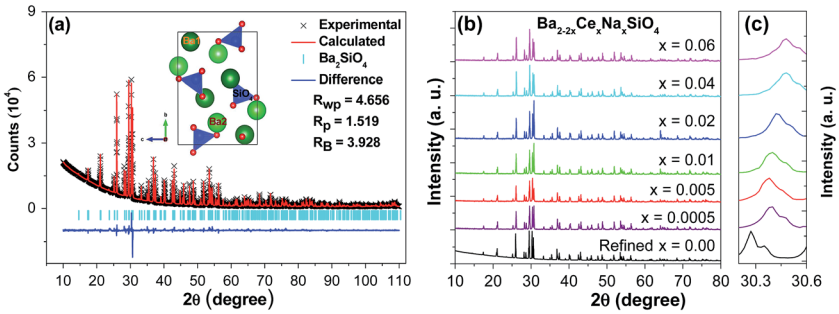

Fig. 1 (a) Rietveld refinement for the powder XRD pattern of the Ba_2SiO_4 host and a depiction of the unit cell structure in the inset. (b) The XRD patterns and (c) diffraction peaks corresponding to (130) crystallographic planes of samples $Ba_{2-2x}Ce_xNa_xSiO_4$ ($x = 0.0005$–0.06). The refined XRD pattern for Ba_2SiO_4 ($x = 0.00$) is also shown as a reference.

temperature of 225 °C.[12] It is noted that, although photoluminescence properties of Ca_2SiO_4:Ce^{3+} have been investigated in relation with the local structure of Ce^{3+},[13] similar studies on the end member Ba_2SiO_4:Ce^{3+} are still lack. Such basic information is important in tailoring Ba_2SiO_4:Ce^{3+}-containing phosphors with desired properties.

In the present work, we extend previous measurements of emission and excitation spectra of Ce-doped Ba_2SiO_4 by using VUV-UV excitations with synchrotron radiation at low temperatures, and then investigate luminescence properties of the compound under X-ray excitation. Hybrid DFT calculations within the supercell model are performed to optimize the local structures of Ce^{3+} located on the Ba1 and Ba2 sites, based on which wave function-based *ab initio* calculations within the embedded cluster model are carried out to derive the $4f^1$ and $5d^1$ energy levels of Ce^{3+}. By comparing the DFT total energies for the Ce_{Ba1}- and Ce_{Ba2}-doped supercells and the calculated and experimental 4f → 5d transition energies, the site occupancy of Ce^{3+} in Ba_2SiO_4 is discussed in association with the local coordination structure. Moreover, electronic properties of Ce^{3+} in Ba_2SiO_4 are also evaluated to understand the thermal stability of the 5d luminescence. The paper is organized as follows. The experimental and computational methods are described in Section 2. The results of luminescence measurements and *ab initio* calculations are presented and discussed in Section 3, with the final conclusions collected in Section 4.

2. Methodology

2.1. Experimental details

Powder samples of $Ba_{2-2x}Ce_xNa_xSiO_4$ ($x = 0.0005$–0.06) were synthesized by the solid-state reaction at high temperature. The starting materials included analytical grade $BaCO_3$, Na_2CO_3, and 99.99% purity SiO_2 and CeO_2, where Na_2CO_3 was used to introduce Na_{Ba} point defects to compensate for the excess charge of Ce^{3+} on the Ba^{2+} site. After being thoroughly mixed in an agate mortar using alcohol as the mixing medium, stoichiometric amounts of the materials were calcined in 10% H_2/90% N_2 reducing atmosphere at 1350 °C for 5 h. The phase purity and crystal structures of the samples were examined by powder X-ray diffraction patterns on a Rigaku D-MAX 2200 VPC X-ray diffractometer with a wavelength of 1.54056 Å Cu Kα radiation at 40 kV and 26 mA. High quality diffraction data of the Ba_2SiO_4 host for the Rietveld refinement were collected over a 2θ range from 10° to 110° at Bruker D8 advanced X-ray diffractometer also with Cu Kα radiation (40 kV and 40 mA), and the refinement was performed using TOPAS-Academic program. The UV-vis excitation and emission spectra as well as the luminescence decay curves were recorded at an Edinburgh FLS-920 combined with a steady-state and fluorescence lifetime spectrometer. The excitation and emission spectra in the VUV-UV range were measured on the beam line 4B8 of the Beijing Synchrotron Radiation Facility (BSRF) under normal operating conditions by using the spectrum of sodium salicylate (o-$C_6H_4OHCOONa$) as a reference.[14] The spectra of X-ray excited luminescence were recorded *via* Ocean Optics QE65000 spectrometer combined with an X-ray tube with tungsten anode as excitation source operating at 90 kV and 5 mA.

2.2. Computational details

The Ce-doped Ba_2SiO_4 crystal was modeled by a $2 \times 1 \times 2$ supercell containing 112 atoms, in which one of the 32 Ba^{2+} ions was replaced by a Ce^{3+} and another by Na^+ for charge compensation, corresponding to the chemical formula $Ba_{2-2x}Ce_xNa_xSiO_4$ ($x \approx 0.0625$). Four different Ce_{Ba}–Na_{Ba} double substitutions were considered, with Ce^{3+} located at a Ba1 or Ba2 site and Na^+ at a nearest-neighbor or distant Ba site within the supercell. The nearest distance between Ce^{3+} ions in the supercell systems is around 10.2 Å, which is large enough to avoid their mutual influence in the computational study of localized electronic states of an individual Ce^{3+}. The lattice parameters and atomic coordinates of the supercells were first optimized by periodic DFT with a hybrid functional in the PBE0 scheme,[15] as implemented in the VASP package.[16,17] The $Ba(5s^25p^66s^2)$, $Si(3s^23p^2)$, $O(2s^22p^4)$, and $Ce(5s^25p^64f^15d^16s^2)$ were treated as valence electrons, and their interactions with the cores were described by the projected augmented wave method.[18] The convergence criteria for total energies and atomic forces were set to 10^{-4} eV and 0.02 eV $Å^{-1}$, respectively, with a cutoff energy of 530 eV for the plane wave basis. One k-point Γ was used to sample the Brillouin zone.

The 4f → 5d transition energies of Ce^{3+} were calculated with a wave function-based embedded cluster approach. The Ce-centered cluster was first constructed on the basis of the DFT-optimized crystal structure, each comprising the central Ce^{3+} and the oxygen ions in the first coordination shell. Its immediate surrounding within a sphere of radius 10.0 Å was represented by several hundreds of *ab initio* model potentials (AIMPs),[19] and the remainder of the surroundings were simulated by tens of thousands of point charges at lattice sites, which were generated with Lepetit's method.[20] Wave function-based CASSCF/CASPT2 calculations with the spin–orbit effect were then carried out to obtain the $4f^1$ and $5d^1$ energy levels of Ce^{3+} by using the program MOLCAS.[21] In the CASSCF calculations, a [4f, 5d, 6s] complete active space was adopted, and in the CASPT2 calculations, the dynamic correlation effects of the Ce^{3+}(5s, 5p, 4f, 5d) electrons and the O^{2-}(2s, 2p) electrons were taken into account. Further details of the calculations can be found in ref. 22 and 23.

3. Results and discussion

3.1. Structural characterization

Rietveld refinement of the XRD pattern of Ba_2SiO_4 was performed, for which the orthorhombic structure (ICSD no. 6246)[11] was employed as the initial model. A comparison of the experimental and calculated results (Fig. 1a) shows that the sample is of single phase without detectable impurities or a second phase. The sample crystallizes in an orthorhombic structure with the space group *Pmcn*, and the lattice parameters were determined to be $a = 5.807$ Å, $b = 10.213$ Å, $c = 7.504$ Å, $V = 445.057$ Å^3. The atomic positions and occupancy factors are listed in Table 1. The average Ba–O bond lengths of the $Ba1O_{10}$ and $Ba2O_9$ coordination polyhedra are 2.985 and 2.826 Å, respectively. The present results for the structure of Ba_2SiO_4 are in good agreement with those reported in ref. 11. For Ce-doped samples, $Ba_{2-2x}Ce_xNa_xSiO_4$ (x = 0.0005–0.06), the XRD patterns are shown in Fig. 1b. No significant impurities peaks can be observed, indicating the Ce^{3+} and Na^+ are completely dissolved into the host. The diffraction peak of (130) crystallographic plane shifts to larger angles as the doping concentration increases (Fig. 1c), which is due to a decrease in the size of the unit cell with increasing dopant content, in light of the smaller ionic sizes of Ce^{3+} and Na^+ than that of Ba^{2+}.[24]

Table 1 The atomic coordinates and occupancy factors for Ba_2SiO_4[a]

Atom	Site	x	y	z	Occupancy
Ba1	4c	0.2500	0.0870	0.1608	1
Ba2	4c	0.2500	0.6955	−0.0084	1
Si	4c	0.2500	0.4200	0.2282	1
O1	4c	0.2500	0.5705	0.3097	1
O2	8d	0.0195	0.3479	0.3051	1
O3	4c	0.0250	0.4159	0.0130	1

[a] $a = 5.80737(3)$ Å, $b = 10.21296(5)$ Å, $c = 7.50385(4)$ Å, $V = 445.057(4)$ Å^3; space group, *Pmcn*; $Z = 4$; $d = 5.47$ g cm^{-3}.

3.2. Photoluminescence properties

Fig. 2 shows the emission and excitation spectra of $Ba_{1.999}Ce_{0.0005}Na_{0.0005}SiO_4$ recorded at low temperatures. In Fig. 2a, the emission spectra were measured at 4 K under excitation at different wavelengths from 315 to 350 nm. All the spectra exhibit two-band profiles with the peak wavelengths almost overlapped with each other. The separations of the two bands are around 1940 cm^{-1}, which is typical of 5d emission from a given kind of Ce^{3+} centers, and can be attributed to the transitions from the lowest excited 5d level to the spin–orbit split $^2F_{5/2}$ and $^2F_{7/2}$ multiplet terms of $4f^1$ configuration. The relative intensities of the emission spectra are in line with those at the excitation wavelengths within the lowest-energy excitation band profile (Fig. 2b). Since the doping concentration is low in the sample under investigation, the energy transfer between Ce^{3+} activators is expected to be inefficient. Thus, the above observations imply that the emissions come predominantly from one kind of Ce^{3+} centers with similar coordination environments. Considering the smaller ionic size of Ce^{3+} than Ba^{2+}, we suppose that the emissions originate from Ce^{3+} centers located at nine-coordinated Ba2 sites rather than ten-coordinated Ba1 sites, as will be confirmed by *ab initio* calculations (see Section 3.3).

Fig. 2b shows four representative VUV-UV excitation spectra of $Ba_{1.999}Ce_{0.0005}Na_{0.0005}SiO_4$ measured at 26.5 K, by monitoring the emission at different wavelengths. The relative intensities of the excitation spectra are consistent with those at the monitoring wavelengths within the emission spectral profile. Each of the spectra consists of four distinct bands at around 327 (band A), 248 (band B), 229 (band C) and 182 nm (band D), and a clear shoulder (A′) on the shorter-wavelength side of the band A. In light of the similarity of the spectral shapes, we assign the band A, B, C and the shoulder A′ to transitions from the ground 4f level to excited 5d levels of a given type of Ce^{3+} centers, presumably located at Ba2 sites. From the maximum energies of the lowest-energy excitation band (A) and the higher-energy emission band, the Stokes shift of the 5d → 4f emission is estimated to be 3843 cm^{-1} (0.48 eV), within the range of those for Ce-doped silicate compounds.[25] The excitation band D at 182 nm (6.81 eV) is attributed to the host excitonic absorption, corresponding to the excitation of an electron from the top of the host valence band to the energetically lowest bound excitonic state. By taking into account the electron–hole binding energy of the exciton,[26] the band gap of the host is estimated to be $\sim 1.08 \times 6.81 = 7.36$ eV.

Fig. 3 shows the decay curves of Ce^{3+} 5d → 4f emission at different wavelengths within the emission profile (Fig. 2a) upon 325 nm excitation of $Ba_{1.999}Ce_{0.0005}Na_{0.0005}SiO_4$ at 4 K. All the curves are overlapped with each other, and can be well fitted by the monoexponential function with lifetimes of about 26 ns, as indicated in the figure. These luminescence decay behaviors at different wavelengths are consistent with the presence of a single type of Ce^{3+} centers in the studied sample.

In addition, we have also measured low-temperature emission and excitation spectra and luminescence decay curves of $Ba_{1.9995}Ce_{0.0005}SiO_4$ without the presence of Na^+ as charge compensators (see Fig. S1 and S2 in ESI†). Comparison of the

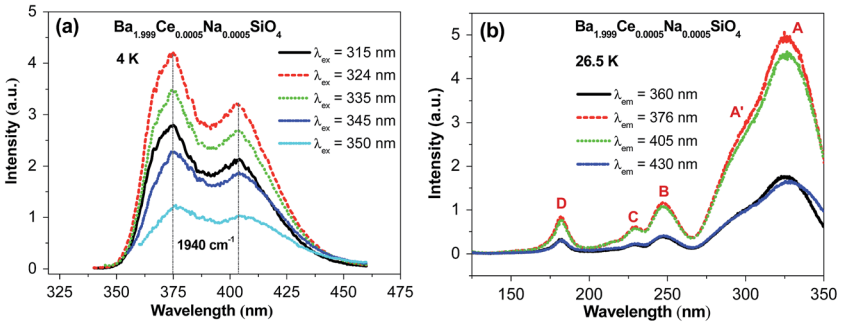

Fig. 2 (a) The UV-vis emission (λ_{ex} = 315, 324, 335, 345, and 350 nm) spectra of $Ba_{1.999}Ce_{0.0005}Na_{0.0005}SiO_4$ at 4 K, and (b) the synchrotron radiation VUV-UV excitation (λ_{em} = 360, 376, 405, and 430 nm) spectra of the sample at 26.5 K.

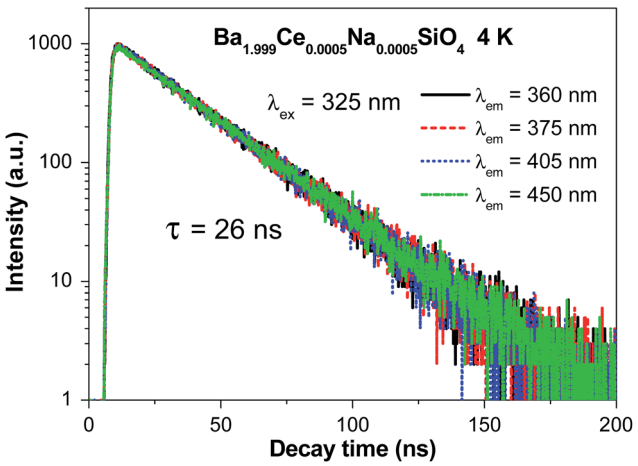

Fig. 3 Luminescence decay curves (λ_{ex} = 325 nm; λ_{em} = 360, 375, 405, and 450 nm) of $Ba_{1.999}Ce_{0.0005}Na_{0.0005}SiO_4$ at 4 K.

results with those for $Ba_{1.999}Ce_{0.0005}Na_{0.0005}SiO_4$ indicates that the presence of Na^+ has no obvious influence on spectral properties of Ce^{3+}, and thus does not affect the occupation of Ce^{3+} at a given type of Ba^{2+} sites. Nevertheless, the addition of Na^+ for charge compensation can lead to a lower concentration of point defects when compared to samples without Na^+. These defects could act as electron–hole recombination centers and hence deteriorate the emission properties of the material.

Fig. 4a displays the emission spectra of $Ba_{1.999}Ce_{0.0005}Na_{0.0005}SiO_4$ upon 325 nm excitation at temperatures from 77 to 500 K. The emission profile becomes more featureless with increasing temperature, which can be ascribed to thermally induced band broadening. The inset shows the CIE chromaticity coordinate of $Ba_{1.999}Ce_{0.0005}Na_{0.0005}SiO_4$, the emission colors at various temperatures all showing the same purple-blue (0.164, 0.013 ± 0.001). In addition, the temperature dependence of the integrated emission intensity is displayed in the right inset of the figure. It shows that from 77 to 500 K only ~4% of the initial intensity is lost, indicating an excellent thermal stability of the phosphor. Fig. 4b gives the decay curves of 376 nm emission under excitation at 325 nm at different temperatures. All the curves exhibit similar monoexponential behaviors, and the derived lifetimes are plotted in the inset of the figure, which shows no luminescence quenching at up to 500 K. Instead, a slight increase in lifetime can be observed, probably due to an enhanced reabsorption at raised temperatures.[27]

3.3. X-ray excited luminescence properties

Considering the fast decay time (~26 ns under UV excitation at 4 K) and excellent thermal stability ($T_{0.5}$ > 500 K) of luminescence in $Ba_{1.999}Ce_{0.0005}Na_{0.0005}SiO_4$, as well as the large density (5.47 g cm^{-3}) and effective atomic number (49.9) of Ba_2SiO_4, we have further evaluated the potential application of Ba_2SiO_4:Ce^{3+} as a scintillation phosphor. Fig. 5 shows a comparison of X-ray

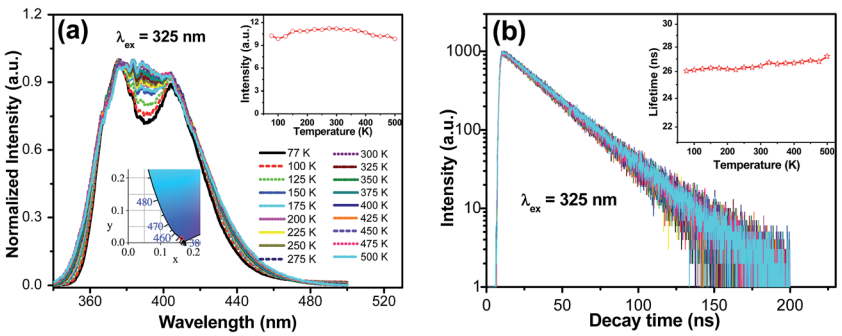

Fig. 4 Temperature-dependence of emission spectra ((a), λ_{ex} = 325 nm) and decay curves ((b), λ_{ex} = 325 nm, λ_{em} = 376 nm) of $Ba_{1.999}Ce_{0.0005}Na_{0.0005}SiO_4$. The CIE chromaticity coordinate of the sample is also shown in the inset.

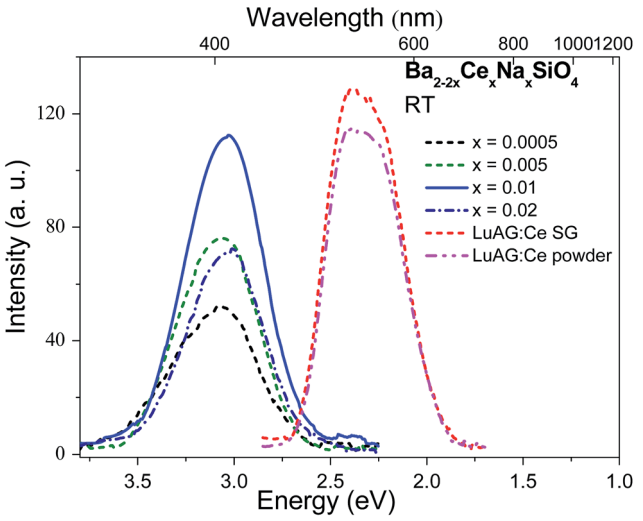

Fig. 5 X-ray excited emission spectra of $Ba_{2-2x}Ce_xNa_xSiO_4$ (x = 0.0005, 0.005, 0.01, and 0.02) and the commercial $Lu_3Al_5O_{12}:Ce^{3+}$ (LuAG:Ce) single crystal (SG) and powder measured at room temperature (RT).

excited luminescence spectra of $Ba_2SiO_4:Ce^{3+}$ and the commercial scintillators $Lu_3Al_5O_{12}:Ce^{3+}$ in single-crystal and powder forms measured at the same experimental conditions. Under X-ray excitation, $Ba_2SiO_4:Ce^{3+}$ samples give broad and featureless emission bands at ~408 nm due to 5d → 4f transitions of Ce^{3+}. This is in line with the room temperature emission spectrum in Fig. 4, with slight difference in emission peaks as a result of detector and instrument responses. By using that of the commercial $Lu_3Al_5O_{12}:Ce^{3+}$ powder (18 000 photon per MeV)[28] as a reference, the absolute light yields for the x = 0.0005, 0.005, 0.01, and 0.02 samples were estimated to be 10 300, 13 500, 19 600 and 12 600 photon per MeV respectively. The large light yield of the x = 0.01 sample implies that $Ba_2SiO_4:Ce^{3+}$ could be a promising scintillation material worth further optimization.

3.4. *Ab initio* calculations

3.4.1. Structural properties. The orthorhombic structure of pure Ba_2SiO_4 was first optimized by using periodic DFT with standard PBE0 hybrid functional that contains 25% Hartree–Fock (HF) exchange. As shown in Table 2, the calculated lattice parameters agree well with experimental data, with the deviations less than 0.79%. The results obtained with the pure PBE functional are also listed in the table for comparison. On the basis of the optimized structure, the band gap energy (E_g) with standard PBE0 is predicted to be 7.09 eV, smaller than the experimentally estimated value of 7.36 eV. By increasing the fraction of HF exchange up to 28% in the PBE0 functional, this experimental E_g value can be reached (calc. 7.38 eV), with the optimized lattice parameters being still in good agreements with experiments (the deviations less than 0.70%). In view of these results, we have employed the above modified PBE0 functional in the following calculations of structural and electronic properties of Ce-doped Ba_2SiO_4 supercells.

Table 2 Calculated and experimental (expt) values for the lattice parameters and the band gap energy of the Ba_2SiO_4 crystal

	a (Å)	b (Å)	c (Å)	E_g (eV)
PBE	5.890	10.407	7.593	4.62
PBE0 (25% HF)	5.833	10.294	7.533	7.09
PBE0 (28% HF)	5.829	10.284	7.524	7.38
Expt	5.807	10.213	7.504	7.36

For Ce,Na-codoped Ba_2SiO_4 supercells, four different Ce_{Ba}–Na_{Ba} double substitutions have been considered, which are distinguished by the shortest (3.793 Å) and longest (7.185 Å) Ba–Ba distances in the undoped supercell. Compared with the undoped supercell, the structural relaxation suggests that the incorporation of Ce_{Ba}–Na_{Ba} causes small decreases (by 0.716–0.944%) in the supercell volume, and slightly distorts the orthorhombic structure of the undoped supercell into monoclinic structures, with the deviations of angles to within ±0.185°. Thus, the calculations predict a negligible deformation of the crystallographic phase when a small amount of Ce and Na are substituted into the Ba sites, in consistence with XRD measurements (Fig. 1b).

Table 3 presents the calculated DFT total energies for the four Ce,Na-codoped supercells. It shows that the two Ce_{Ba2}–Na_{Ba1} substitutions are much more stable than the two Ce_{Ba1}–Na_{Ba2} (by at least 670 meV), irrespective of the Ce–Na distance. For a given Ce_{Ba}–Na_{Ba} combination, the two single substitutions prefer to be close to each other, as is expected from their opposite effective charges. The relative stabilities may be qualitatively understood by the valences of Ce^{3+} and Na^+ calculated from their optimized local structures using the bond valence sum (BVS) method.[29] The results are listed in the last two columns of Table 3. It shows that the BVS values of Ce^{3+} at the Ba2 site are much closer to the formal value (+3) than those of Ce^{3+} at the Ba1 site; the same is true for Na^+. This suggests that the greater stability of Ce_{Ba2}–Na_{Ba1} than Ce_{Ba1}–Na_{Ba2} is due to the preference of Ce^{3+} at the Ba2 site over the Ba1 site. This point is further supported by the calculated DFT total energies for the optimized supercells with a single Ce^{3+} (Na^+) substituted at the Ba1 or Ba2 site, with the net defect charge compensated by a uniform charge density. The results show that the Ce_{Ba2} (Na_{Ba2}) substitution is energetically more favorable by 979 meV (118 meV) than the Ce_{Ba1} (Na_{Ba1}) substitution, consistent with the above BVS analysis.

The local structures of Ce^{3+} in the optimized supercells are depicted in Fig. 6, with the values of selected relaxed (unrelaxed) bond lengths indicated. All the Ce_{Ba} substitutions cause decreases in the average bond length by 0.054–0.158 Å, consistent with the smaller ionic size of Ce^{3+} than Ba^{2+}. The local structural distortion around Ce_{Ba1} is more severe than that around Ce_{Ba2}. Specifically, the bond distances from Ce_{Ba1} (Ce_{Ba2}) to the six (seven) nearest O atoms are decreased by 0.242–0.487 Å (0.148–0.342 Å), whereas to the four (two) farthest O atoms, the distances are increased by 0.114–0.565 Å (0.147–0.154 Å), presumably due to steric repulsion. It also shows that

Table 3 Calculated total energies for Ce,Na-codoped Ba_2SiO_4 supercells. The Ce–Na distances (d in Å) in the unrelaxed and optimized supercells are also included

	d (Å)		Total energy (eV)	Relative total energy (meV)	Valence by BVS	
	Unrelaxed	Optimized			Ce	Na
Ce_{Ba2}–Na_{Ba1}	3.793	3.333	−1029.4551	0	2.759	0.698
Ce_{Ba2}–Na_{Ba1}	7.185	6.972	−1029.3598	95	2.711	0.605
Ce_{Ba1}–Na_{Ba2}	3.793	3.642	−1028.6900	765	2.636	0.916
Ce_{Ba1}–Na_{Ba2}	7.185	6.977	−1028.1342	1321	2.259	0.882

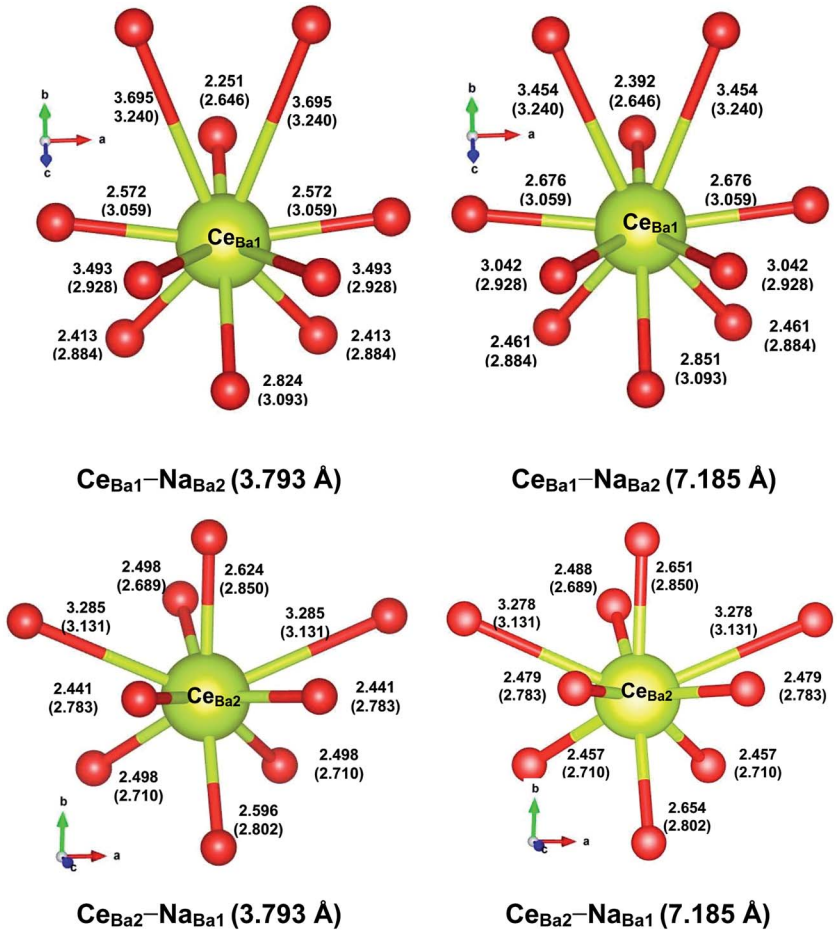

Fig. 6 DFT-optimized local coordination structures of Ce at the Ba1 and Ba2 sites. The relaxed (unrelaxed) Ce–O distances (Å) are indicated.

the nearby Na^+ has a more pronounced effect on the local structures of Ce_{Ba1} than that of Ce_{Ba2}, when compared with their respective local structures with a distant Na^+ present. This indicates that the local structure of Ce_{Ba2} is more rigid than that of Ce_{Ba1}, which could be correlated with greater stability of the former substitution than the later.

3.4.2. 4f → 5d transitions of Ce^{3+}. On the basis of the DFT-optimized structures for Ce,Na-doped Ba_2SiO_4 supercells, Ce-centered embedded clusters, $(Ce_{Ba1}O_{10})^{17-}$ and $(Ce_{Ba2}O_9)^{15-}$, were constructed, with their surroundings simulated by AIMPs and point charges at lattice sites. Wave function-based CASSCF/CASPT2 calculations at the spin–orbit level were performed to obtain the $4f^1$ and $5d^1$ energy levels of Ce^{3+}, and the results are given in Table 4. We note that, for Ce^{3+} at the Ba1 (Ba2) site, the two sets of $5d^1$ energy levels obtained in the presence of a nearby or a distant Na^+ are quite different from (close to) each another, with absolute average deviations of 2712 cm^{-1} (464 cm^{-1}). This is consistent with the above analysis of the effect of Na^+ position on the local structures of Ce^{3+} (see Section 3.4.1), considering the strong crystal field interaction of the Ce^{3+} 5d electron with the local environment.

To facilitate comparison with experimental excitation spectra, the calculated $4f_1 \rightarrow 5d_i$ (i = 1–5) transitions are schematically presented in Fig. 7, where the relative transition

Table 4 Calculated $4f^1$ and $5d^1$ energy levels for Ce-centered embedded clusters in Ba_2SiO_4 using the CASSCF/CASPT2 method at the spin–orbit level. The values in parentheses of the second row indicate the unrelaxed Ce–Na distances

	Ce_{Ba1}–Na_{Ba2} (3.793 Å)	Ce_{Ba1}–Na_{Ba2} (7.185 Å)	Ce_{Ba2}–Na_{Ba1} (3.793 Å)	Ce_{Ba2}–Na_{Ba1} (7.185)
$4f_1$	0	0	0	0
$4f_2$	679	398	472	411
$4f_3$	1066	496	863	671
$4f_4$	2259	2230	2325	2343
$4f_5$	2948	2585	2647	2572
$4f_6$	3034	2710	3172	2892
$4f_7$	3599	2941	3340	3223
$5d_1$	32 391	35 856	30 445	30 886
$5d_2$	33 740	36 968	31 870	32 069
$5d_3$	37 599	40 571	42 534	41 937
$5d_4$	46 380	46 260	46 304	45 774
$5d_5$	54 605	50 830	51 951	52 504

intensities within each cluster were calculated using the wave functions and energies at the spin–orbit level. It is apparent from the figure that the experimental excitation spectrum can be assigned to the $4f_1 \rightarrow 5d_i$ transitions of Ce^{3+} located at Ba2 sites. The lowest excitation band (band A, Fig. 7a) can be clearly ascribed to $4f_1 \rightarrow 5d_1$ transitions of $Ce_{Ba2}{}^{3+}$, and the shoulder (A′) on the shorter wavelength side to $4f_1 \rightarrow 5d_2$ transitions. The two higher excitation bands, *i.e.*, bands B and C, can be attributed to $4f_1 \rightarrow 5d_{3,4}$ transitions, respectively, but with an average underestimation of about 2140 cm^{-1}. Thus, the above comparison provides direct evidence for the predominant preference of the dopant Ce^{3+} for the nine-coordinated Ba2 site over the ten-coordinated Ba1 site, which is also in consistence with the results of DFT total energy calculations.

3.4.3. Electronic properties. Fig. 8 depicts calculated total and orbital projected density of states (DOSs) of the supercell containing the stable Ce_{Ba2}–Na_{Ba1} (3.793 Å) substitution. It shows that the top of the host valence band is dominated by O 2p states with a dispersion of ~6.0 eV, while the bottom of host conduction band is mainly composed of Ba 5d states. The double substitution leads to the formation of an occupied 4f state deep inside the host band gap (indicated by the dashed line in the figure), in correspondence to a lone Ce^{3+} 4f electron. This occupied 4f state resides at ΔE_{4f} = 1.53 eV above the valence band maximum (VBM) of the host.

It is worth stressing that ΔE_{4f} was derived in the single particle approximation of DFT (Kohn–Sham eigenvalues), and a more rigorous determination of the energy position of the occupied Ce^{3+} 4f state requires to calculate the charge transition level.[30] The Ce-induced charge transition level $\varepsilon(Ce^{3+/4+})$ with reference to the host VBM is defined as the Fermi level at which the defect formation energies of Ce^{3+} and Ce^{4+} are equal to each other, and can be computed using

$$\varepsilon(Ce^{3+/4+}) = E_{tot}(Ce^{3+}) - E_{tot}(Ce^{4+}) - \varepsilon_{VBM}$$

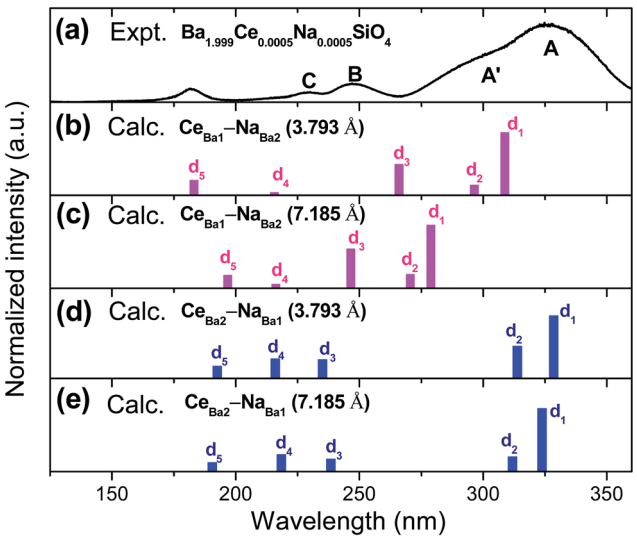

Fig. 7 Schematic representation of the calculated energies and relative intensities of the $4f_1 \rightarrow 5d_i$ (i = 1–5) transitions of Ce^{3+} on the Ba^{2+} sites of Ba_2SiO_4. The VUV-UV excitation spectrum of $Ba_{1.999}Ce_{0.0005}Na_{0.0005}SiO_4$ (λ_{em} = 376 nm) at 26.5 K (see also Fig. 2b) is also shown for comparison.

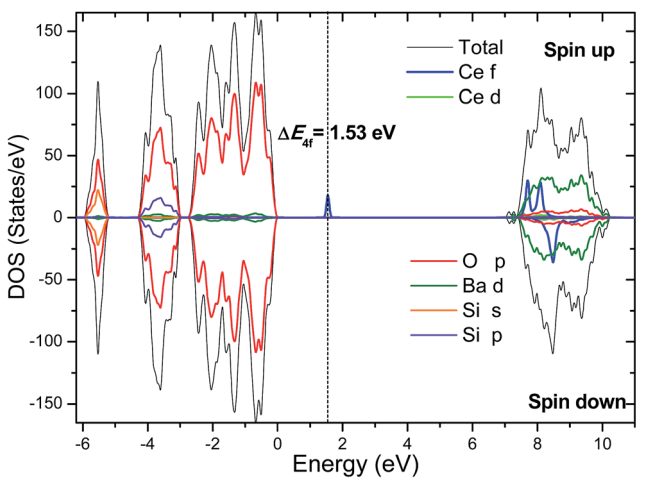

Fig. 8 Calculated total and orbital projected DOSs for the Ba_2SiO_4 supercell with the Ce_{Ba2}–Na_{Ba1} (3.793 Å) substitution. The occupied Ce^{3+} 4f state is indicated by the dashed line, and its energy position with respect to the host VBM is indicated.

where E_{tot} is the total energies of the relaxed structure of the supercell containing Ce^{3+} or Ce^{4+}, and ε_{VBM} is the energy of the host VBM. The predicted value for $\varepsilon(Ce^{3+/4+})$ is 2.44 eV, which also means that the thermal ionization energy of Ce^{3+} into Ce^{4+} is $E_{gap} - \varepsilon(Ce^{3+/4+}) = 4.92$ eV, as could be determined, for example, from photoconductivity measurements.[31]

Given the value of $\varepsilon(Ce^{3+/4+})$, the energy difference (ΔE_{5d1}) between the lowest Ce^{3+} $5d_1$ level and the conduction band minimum (CBM) of the host can also be estimated by

$$\Delta E_{5d1} = E_{gap} - [\varepsilon(Ce^{3+/4+}) + \Delta E(4f_1 \rightarrow 5d_1) - (1/2)\Delta E_{SS}]$$

where $\Delta E(4f_1 \rightarrow 5d_1)$ is the lowest $4f_1 \rightarrow 5d_1$ transition energy of Ce^{3+} and ΔE_{SS} is the Stokes shift. From the values of E_{gap} (7.36 eV), $\Delta E(4f_1 \rightarrow 5d_1)$ (3.79 eV), and ΔE_{SS} (0.48 eV), the value of ΔE_{5d1} is estimated to be 1.37 eV, corresponding to a thermal quenching temperature ($T_{0.5}$) of 932 K on the basis of a crude relationship between ΔE_{5d1} and $T_{0.5}$, *i.e.*, $T_{0.5} = 680 \times \Delta E_{5d1}$.[32] This is in qualitative agreement with the experimental result (see Section 3.2) that luminescence quenching was not yet observed when the temperature was raised up to 500 K.

4. Conclusions

We have investigated photoluminescence properties of Ce-doped Ba_2SiO_4 from a combination of experimental and theoretical methods. Under UV excitation, the compound $Ba_{1.999}Ce_{0.0005}Na_{0.0005}SiO_4$ exhibits bright luminescence at 350–450 nm, with a fast decay time (~26 ns) and a high thermal quenching temperature (>500 K). The X-ray excited luminescence measurements were then conducted, and a comparison of the results with those of the commercial LuAG:Ce^{3+} suggests a potential application of Ba_2SiO_4:Ce^{3+} as scintillation phosphors. The VUV-UV excitation spectra obtained for $Ba_{1.999}Ce_{0.0005}Na_{0.0005}SiO_4$ by monitoring emission at different wavelengths at low temperature revealed that the emission originates predominantly from Ce^{3+} located at one type of Ba sites. This was found to be the nine-coordinated Ba2 site, on the basis of computations using hybrid DFT and wave function-based *ab initio* methods. In addition, the energy location of Ce^{3+} 4f and $5d_1$ states within the host band gap was derived theoretically, and the large energy separation (~1.37 eV) between the $5d_1$ state and the host CBM is consistent with the high thermal stability of the 5d luminescence as observed experimentally. The present work also demonstrate that low-temperature excitation spectral measurements in combination with elaborate *ab initio* calculations are able to offer microscopic insight into the structure–property relationship of Ce^{3+} in a local environment of low symmetry, which is common in Ce-activated phosphors for practical applications.

Acknowledgements

The work is financially supported by the National Natural Science Foundation of China (21671201, 11574003, U1432249, and U1632101). Technical assistance of the X-ray excited luminescence measurement Yihong Qi, Yangbing Xu, and Prof. Kai Wang from SYSU-CMU Joint Institute of Engineering is gratefully acknowledged.

Notes and references

1 W. M. Yen, A. Shionoya and H. Yamamoto, *Phosphor Handbook*, CRC Press, Boca Raton, FL, 2007.
2 Y. Li, J. Wang, X.-M. Wang, F. Pan, T. Zhou and R.-J. Xie, *J. Mater. Chem. C*, 2017, **5**, 1022.
3 D. Wen, H. Kuwahara, H. Kato, M. Kobayashi, Y. Sato, T. Masaki and M. Kakihana, *ACS Appl. Mater. Interfaces*, 2016, **8**, 11615.
4 Z. Xia, S. Miao, M. Chen, M. S. Molokeev and Q. Liu, *Inorg. Chem.*, 2015, **54**, 7684.
5 Z. Hao, J. Zhang, X. Zhang, Y. Luo, L. Zhang and H. Zhao, *J. Lumin.*, 2014, **152**, 40.
6 T. L. Barry, *J. Electrochem. Soc.*, 1968, **115**, 1181.
7 P. V. Kelsey and J. J. Brown, *J. Electrochem. Soc.*, 1976, **123**, 1384.
8 K. A. Denault, J. Brgoch, M. W. Gaultois, A. Mikhailovsky, R. Petry, H. Winkler, S. P. DenBaars and R. Seshadri, *Chem. Mater.*, 2014, **26**, 2275.
9 A. Kalaji, M. Mikami and A. K. Cheetham, *Chem. Mater.*, 2014, **26**, 3966.
10 P. Dorenbos, *Phys. Rev. B: Condens. Matter Mater. Phys.*, 2001, **64**, 125117.
11 H. Grosse and E. Tillmanns, *Cryst. Struct. Commun.*, 1974, **3**, 599.
12 K. Park, J. Kim, P. Kung and S. M. Kim, *J. Lumin.*, 2010, **130**, 1292.
13 Y. Liu, Q. Fang, L. Ning, Y. Huang, S. Huang and H. Liang, *Opt. Mater.*, 2015, **44**, 67.
14 Y. Tao, Y. Huang, Z. Gao, H. Zhuang, A. Zhou, Y. Tan, D. Li and S. Sun, *J. Synchrotron Radiat.*, 2009, **16**, 857.
15 J. P. Perdew, M. Ernzerhof and K. Burke, *J. Chem. Phys.*, 1996, **105**, 9982.
16 G. Kresse and J. Furthmuller, *Phys. Rev. B: Condens. Matter Mater. Phys.*, 1996, **54**, 11169.
17 G. Kresse and D. Joubert, *Phys. Rev. B: Condens. Matter Mater. Phys.*, 1999, **59**, 1758.
18 P. E. Blöchl, *Phys. Rev. B: Condens. Matter Mater. Phys.*, 1994, **50**, 17953.
19 Z. Barandiarán and L. Seijo, *J. Chem. Phys.*, 1988, **89**, 5739.
20 A. Gellé and M. B. Lepetit, *J. Chem. Phys.*, 2008, **128**, 244716.
21 G. Karlström, R. Lindh, P.-Å. Malmqvist, B. O. Roos, U. Ryde, V. Veryazov, P.-O. Widmark, M. Cossi, B. Schimmelpfennig and P. Neogrady, *Comput. Mater. Sci.*, 2003, **28**, 222.
22 A. B. Muñoz-García and L. Seijo, *Phys. Rev. B: Condens. Matter Mater. Phys.*, 2010, **82**, 184118.
23 L. Ning, X. Huang, J. Sun, S. Huang, M. Chen, Z. Xia and Y. Huang, *J. Phys. Chem. C*, 2016, **120**, 3999.
24 R. D. Shannon, *Acta Crystallogr., Sect. A: Cryst. Phys., Diffr., Theor. Gen. Crystallogr.*, 1976, **32**, 751.
25 P. Dorenbos, *J. Lumin.*, 2005, **111**, 89.
26 P. Dorenbos, *J. Lumin.*, 2000, **91**, 155.
27 V. Bachmann, C. Ronda and A. Meijerink, *Chem. Mater.*, 2009, **21**, 2077.

28 M. Nikl, A. Yoshikawa, K. Kamada, K. Nejezchleb, C. Stanek, J. Mares and K. Blazek, *Prog. Cryst. Growth Charact. Mater.*, 2013, **59**, 47.
29 N. Brese and M. O'keeffe, *Acta Crystallogr., Sect. B: Struct. Sci.*, 1991, **47**, 192.
30 C. Freysoldt, B. Grabowski, T. Hickel, J. Neugebauer, G. Kresse, A. Janotti and C. G. Van de Walle, *Rev. Mod. Phys.*, 2014, **86**, 253.
31 C. Pédrini, *Phys. Status Solidi A*, 2005, **202**, 185.
32 P. Dorenbos, *J. Phys.: Condens. Matter*, 2005, **17**, 8103.